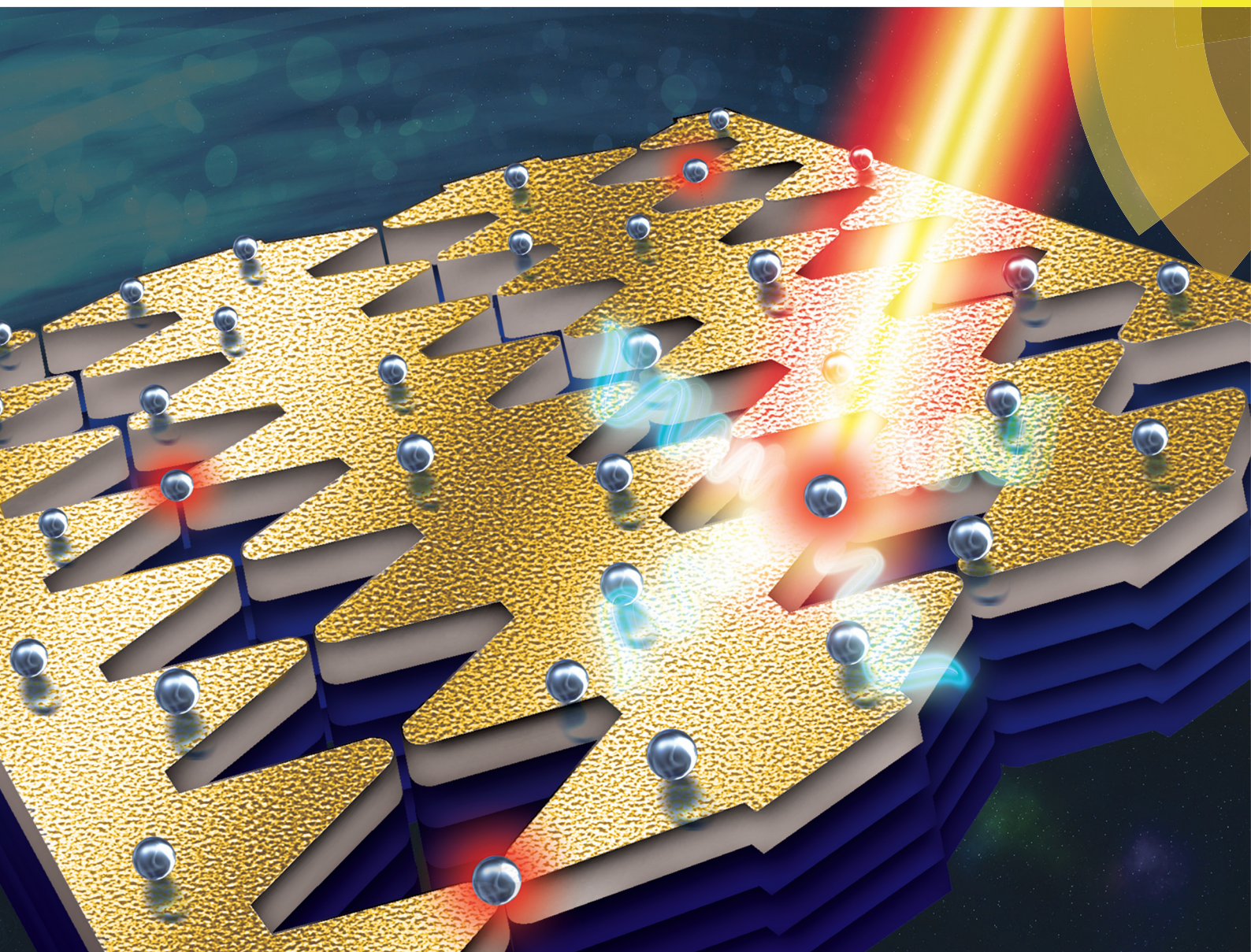# Nanoscale

ROYAL SOCIETY
OF CHEMISTRY

PAPER
Changzhi Gu, Junjie Li *et al.*
Nanocracking and metallization doubly defined large-scale 3D plasmonic
sub-10 nm-gap arrays as extremely sensitive SERS substrates

NCNST

Check for updates

Nanocracking and metallization doubly defined large-scale 3D plasmonic sub-10 nm-gap arrays as extremely sensitive SERS substrates

Ruhao Pan,[a,b] Yang Yang,[a] Yujin Wang,[a] Shuang Li,[b,c] Zhe Liu,[a] Yewang Su, [c] Baogang Quan,[a] Yunlong Li,[a] Changzhi Gu*[a,b,d] and Junjie Li *[a,b]

Considering the technological difficulties in the existing approaches to form nanoscale gaps, a convenient method to fabricate three-dimensional (3D) sub-10 nm Ag/SiN_x gap arrays has been demonstrated in this study, controlled by a combination of stress-induced nanocracking of a SiN_x nanobridge and Ag nanofilm deposition. This scalable 3D plasmonic nanogap is specially suspended above a substrate, having a tunable nanogap width and large height-to-width ratio to form a nanocavity underneath. As a surface-enhanced Raman scattering (SERS) substrate, the 3D Ag/SiN_x nanogap shows a large Raman enhancement factor of $\sim 10^8$ and extremely high sensitivity for the detection of Rhodamine 6G (R6G) molecules, even down to 10^{-16} M, indicating an extraordinary capability for single-molecule detection. Further, we verified that the Fabry−Perot resonance occurred in the deep SiN_x nanocavity under the Ag nanogap and contributed prominently to a tremendous enhancement of the local field in the Ag-nanogap zone and hence ultrasensitive SERS detection. This method circumvents the technological limitations to fabricate a sub-10 nm metal nanogap with unique features for wide applications in important scientific and technological areas.

Introduction

Metallic nanogaps have attracted significant attention in recent years owing to their applicability in physics, chemistry, life sciences, and environmental engineering.[1–5] They are widely used as fundamental building blocks of microelectronic components such as ultrafast vacuum transistors, ultralow-power nanoelectromechanical switches,[6] and metallic-nanogap-electrode-based flexible electronics.[7] In addition, metallic nanogaps are promising for super-resolution imaging,[8] molecular electronic,[5,9,10] and sensor[11–13] applications. Among the diverse applications of metallic nanogaps, surface enhanced Raman spectroscopy (SERS) is one of the most important applications. SERS is a powerful analysis technique for ultra-sensitive detection.[14–22] SERS performance is governed by strong localized surface plasmon resonance

(LSPR) on noble metal nanoparticles or nanopatterns.[12,23–25] Normally, the SERS enhancement factor (EF) of nanopatterns prepared by regular nanofabrication methods is just in the range of 10^5–10^6,[26,27] which is not sufficient for single-molecule detection ($\sim 10^7$).[28] It has been shown that a metallic nanogap can be capable of single-molecule detection.[17–19,29] A sub-10 nm nanogap – wherein the electromagnetic field is strongly coupled in the narrow space, giving rise to a very intense LSPR – is especially suitable for this type of detection. Dimers and even multimeric structures with sub-10 nm nanogaps have been realized by self-assembly of nanoparticles.[30] Recently, a sub-10 nm Au bowtie nanoantenna[18] and a split-wedge antenna 3D nanostructure[31] have been fabricated and reported, achieving an SERS EF of the order of 10^7, which is shown to be capable of single-molecule detection. However, the detection limit for molecule concentration in these reports was normally around 10^{-10} M. Therefore, it is desirable to develop an SERS surface with an even lower detection limit for high sensitivity and fast analysis at ultralow concentration to design and fabricate a better plasmonic nanogap.

Despite the advantages of plasmonic nanogaps and their wide applicability nowadays, a remaining challenge is to fabricate scalable, reliable, and reproducible sub-10 nm metallic nanogaps. Traditional planar fabrication processes, such as ultraviolet lithography (UVL) and electron beam lithography

[a]Beijing National Laboratory for Condensed Matter Physics, Institute of Physics, Chinese Academy of Sciences, Beijing 100190, China. E-mail: jjli@iphy.ac.cn, czgu@iphy.ac.cn; Tel: +86-10-82649097
[b]School of Physical Sciences, CAS Key Laboratory of Vacuum Physics, University of Chinese Academy of Sciences, Beijing 100049, China
[c]State Key Laboratory of Nonlinear Mechanics, Institute of Mechanics, Chinese Academy of Sciences, Beijing 100190, China
[d]Collaborative Innovation Center of Quantum Matter, Beijing, China

(EBL), have sub-micron and 10 nm limitations, respectively.[12] Various methods have been developed to realize nanogaps in the sub-10 nm scale; one effective method uses metallic particles or two-dimensional (2D) thin films to build nanogaps.[32,33] That is, the formation of sub-10 nm gaps should be enabled by graphene,[34] metal particles,[15,35] or self-assembly.[36] However, these methods lack controllability, flexibility, and stability; moreover, they result in chemical pollution. To overcome these drawbacks in nanogaps based on nanoparticles, we had fabricated a metal–insulator-metal (MIM) structure *via* atomic layer deposition (ALD), controlling gap width by tuning the thickness of insulating inter-layer. The aim was to use this device for SERS measurement.[31] However, this type of filled nanogap does not function well as an electrode; this limits the utilization of the nanogap that serves as nanodevices combining multiple functions[37] such as molecule trapping and detection by tunneling current and highly sensitive molecule identification by SERS. Recently, a new form of sub-10 nm gap has appeared, namely, crack- or break-induced nanogaps. A number of methods, including the mechanical break-junction method,[38] swelling-defined nanogaps,[7] and optical breakdown,[39] have been put forward based on the cracking or breaking procedures. Scalable nanogap electrodes were fabricated on flexible substrates by swelling-induced cracks.[7] Note that the gap width in this case is over 50 nm, which is already beyond the scope of plasmon coupling. An approach called the crack-junction (CJ) method was introduced to achieve nanogap arrays over a large area.[40] However, in addition to the inability to control the morphology of tips, the materials used for fabrication must be brittle; this limits the application of the resulting nanogaps. Although many creative methods have been proposed to fabricate nanogaps that offer good performance in either field enhancement or electron transport, parallel fabrication of a stable and scalable sub-10 nm nanogap with control of the shape and width remains a challenge.

Herein, we introduced a convenient stress-induced cracking method to fabricate a suspended 3D sub-10 nm Ag/SiN$_x$ gap consisting of an opposed pair of uniform tips, with good homogeneity over a large area. Each of the Ag/SiN$_x$ nanogaps was fabricated based on stress-induced cracking of a SiN$_x$ nanobridge combined with a metallization process that included EBL and physical and chemical etching techniques, followed by deposition of a Ag nanolayer that could easily tune the location and width of the nanogap. This method circumvents the technological difficulties of the existing ways towards the fabrication of nanoscale gaps. The suspended 3D Ag/SiN$_x$ nanogaps exhibit some unique features such as highly controllable gap width within a range from sub-10 nm to tens of nanometers, high ratio of gap-depth to gap-width, good array scalability, and wafer-scale fabrication. Moreover, we demonstrated ultra-high SERS sensitivity of this suspended 3D metallic sub-10 nm nanogap, and the detection limit of Rhodamine 6G (R6G) molecules was found to be as low as 10^{-16} M and exceeded ~10^8 in the SERS enhancement factor (EF), sufficient for single-molecule detection. Finite-difference time-domain (FDTD) simulation elucidated that the Ag-nanogap, being sub-

10 nm, contributed greatly to a tremendous local field enhancement for SERS. Furthermore, the as-obtained outstanding SERS EF is closely associated with the Fabry–Perot resonances that occur in the deep SiN$_x$ nanocavity under the Ag nanogap. Thus, we have proposed a feasible route to fabricate a large-area uniform 3D sub-10 nm nanogap array with a high SERS enhancement factor for promising applications in ultra-high sensitivity molecule sensing; hence, the more unique features of this nanoarray can be extended to many scientific and technological fields.

Experimental

Fabrication process

The 220 nm thick SiN$_x$ was deposited on a clean Si substrate by low-pressure chemical vapor deposition (LPCVD) with a gas flow of NH$_3$: 30 sccm and SH$_2$Cl$_2$: 120 sccm at 900 °C. Then, 200 nm thick PMMA was spin-coated on SiN$_x$, and EBL (Ratih 150) was introduced to expose the nanobridge pattern. After this, RIE (NGP80, Oxford) was used to etch the PMMA pattern into the SiN$_x$ layer, in which the gas flow was CHF$_3$: 50 sccm and O$_2$: 5 sccm, and the pressure was maintained at 35 mTorr. SiN$_x$ was etched under a power of 200 W at 10 °C for 4 minutes. Then, the sample was dipped in the buffered oxide etching liquid (BOE) for 20 s to remove the oxide layer on the sample; after this, the sample was cleaned with deionized water. TMAH (25% w/w, Alfa Aesar) was heated to 95 °C in an oil bath and kept for 1 hour to allow the temperature to stabilize. Then, the sample was etched by TMAH for 2 min, and finally, the suspended sub-10 nm nanogaps were obtained. The widths of the nanogaps were measured using SEM (Helios 600i, FEI). A silver film was deposited onto the SiN$_x$ nanogap by a magnetron sputtering system with an ultra-high background vacuum (~10^{-10} Torr) to fabricate a metallic nanogap.

Simulation methods

The simulation of nanobridge breaking was based on the finite element method (FEM). The nanobridge chosen for simulation has a width of 20 nm, but the length is set to zero to facilitate simulation. Using FEM together with the maximum normal stress strength theory, the maximum principle stress distribution was given, and the displacement distribution after stress release was calculated. Moreover, the Finite-difference time-domain (FDTD) method was employed to simulate the electric field distribution of the nanogaps. The Ag layer is 25 nm thick, whereas the thickness of the SiN$_x$ layers ranged from 50 nm to 500 nm. The wavelength of the incidence light was set at 532 nm and propagated along the z-axis with the electric field polarized along the x-axis. Herein, three monitors were placed perpendicular to the x, y, and z axes to fully capture the field distribution. All the simulated boundaries were perfectly matched layers (PML) to avoid reflections. Taking advantage of the abovementioned model, the field distribution of the Ag nanogap and the Ag/SiN$_x$ gap on the Si substrate was calculated.

SERS measurements

R6G powders were dissolved in deionized water to prepare the solutions of R6G. The samples were functionalized with molecules by immersion in the solutions for a certain time. The samples were taken out, washed with ethylalcohol and DI water to remove the unbound molecules, and then dried using a flow of nitrogen. The SERS measurements were carried out using a micro-Raman spectrometer (Horiba/Jobin Yvon HR 800) equipped with a 532 nm laser as the excitation source. The laser was focused on the sample surface using a 100× lens (N_A = 0.9) with a size of 2 μm. To protect the molecules from laser heating, the laser power was kept at 1 mW on the sample surface, and the exposure time was 1 second. Each Raman spectrum was obtained for a single gap, and repeatability was verified by obtaining the spectra for 5 randomly chosen gaps in different arrays.

Results and discussion

Doubly controlled fabrication of Ag/SiN$_x$ nanogap arrays

Our fabrication process employing stress-induced cracking starts with the deposition of an amorphous SiN$_x$ film on a Si substrate. A schematic of the process from nanobridge to nanogap is shown in Fig. 1a. At first, a 220 nm amorphous SiN$_x$ layer has been specifically selected and deposited on a Si
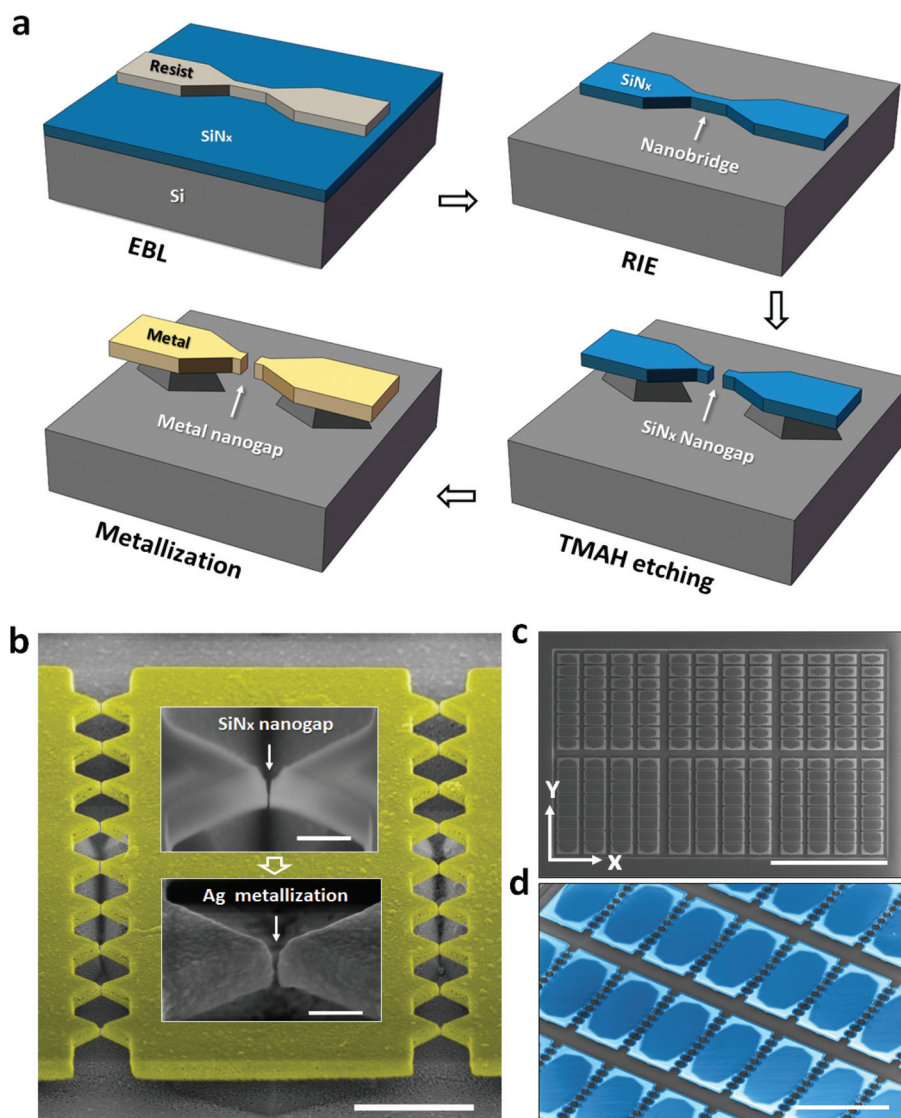
Fig. 1 The stress-induced cracking and metallization doubly controlled method for nanogap fabrication. (a) A schematic of the fabrication process from nanobridge to 3D nanogap by EBL, RIE, TMAH etching, and Ag metallization. (b) An SEM image of two neighboring typical Ag/SiN$_x$ nanogap arrays, in which the two insets present enlarged views of a single SiN$_x$ nanogap before and after Ag coating. The scale bar is 3 μm, and that in the insets is 200 nm. (c) The SEM image of a unit of the SiN$_x$ nanogap arrays in the as-fabricated sample with an area of 1 × 1 cm^2, which includes many nanogap arrays of various sizes depending upon the nanobridge shape. The scale bar is 100 μm. (d) An enlarged SEM image of a section of SiN$_x$ nanogap arrays in (c), and each array includes 9 nanogaps. Scale bar is 10 μm.

substrate because this thick layer will not bend much during the subsequent technical processing of the metal/SiN$_x$ film. The nanobridge pattern was fabricated by an EBL process, and then, the pattern was transferred onto the SiN$_x$ film to serve as a mask during reactive ion etching (RIE). After this, tetramethylammonium hydroxide (TMAH) was used to etch the Si substrate alongside and underneath the SiN$_x$ nanobridge to form a suspended 3D nanobridge. As a result of the concentrated stress-release-induced cracking, a 3D suspended nanogap appeared in the middle of the SiN$_x$ nanobridge, having a width range from sub-10 nm to tens of nanometers. Finally, metallization was accomplished by magnetron sputtering disposition to functionalize the nanogap. During the deposition, the nanogap can be narrowed to sub-10 nm from tens of nanometers. This approach for fabricating nanogaps has better control of the nanogap width and is compatible with typical micro/nanofabrication processes for Si wafers. Thus, it is well suited for the preparation of large-area and customized nanogap arrays, making nanogap-based devices interesting for a wide range of possible applications. Fig. 1b presents an SEM image of the typical as-fabricated metallic nanogap arrays, with two inset SEM images of a single SiN$_x$ nanogap obtained before and after metallization, in which the morphology and width of each metallic nanogap are nearly the same; this demonstrates good scalability and uniformity of the fabrication process employed in this study. Another important feature is that this 3D plasmonic nanogap has a high ratio of gap-depth to gap-width, which can be more than 30 at the sub-10 nm gap to form a nanocavity, benefitting local field enhancement and strong localized surface plasmon resonance.

Fig. 1c shows a typical unit of SiN$_x$ nanogap arrays in a large-scale SiN$_x$ nanogap array sample with an area of 1 × 1 cm^2, which can be easily expanded to larger wafers with distributed multigroup units, each group having an array of nanogaps with different sizes. This suggests mass-fabrication capability. As shown in Fig. 1c, the length and width of each nanobridge is designed to be increased and decreased along the marked arrow direction of X and Y to tune the shape of the original nanobridges individually. The nanobridge shape can be used to control the nanogap width from above 50 nm to sub-10 nm in appropriate locations, at which the TMAH etching process determines the cracking effect and hence the width of the nanogap. In addition, this 3D nanogap can be customized on demand and reused by wet-etching the metal layer away. An enlarged SEM image of a section of nanogap arrays is exhibited in Fig. 1d, in which each array includes 9 nanogaps, and the bright color area on the edge of rectangular unit are corresponding to the suspending SiN$_x$ layer caused by etching process. We can see that the abovementioned fabrication process has good design controllability in a large area with exact location and number of nanogaps and thus enables scalable and customized fabrication.

In the abovementioned schematic of the fabrication process, we can see that the suspended SiN$_x$ nanogap is the framework of the metallic nanogap; thus, control during the fabrication of the SiN$_x$ structure determines the subsequent form of the metallic nanogap. From nanobridge to nanogap, the TMAH etching process is key to produce the suspending, which leads to the release of tensile stress that is inherent in the SiN$_x$ nanobridge. Moreover, this causes the concentrated stress in the middle of the SiN$_x$ nanobridge. Once the local stress in the middle overcomes the strength of the SiN$_x$ film, a crack appears in the middle of the nanobridge. Fig. 2a shows an SEM image of a SiN$_x$ nanobridge with fixed width and length before the TMAH etching process; thus, no nanogap appears. For this unsuspended SiN$_x$ nanobridge, a simulation of stress distribution based on maximum principal stress was carried out by the finite element method (FEM), as shown in Fig. 2b. We can see that the stress is concentrated at the center of the nanobridge; this suggests that the most likely breaking site is on the nanobridge. As a result of the stress released during TMAH etching, the nanogap appears in the middle of the nanobridge, as shown in Fig. 2c, which is the SEM image of a typical array of suspended SiN$_x$ nanogaps induced by the released stress. In Fig. 2c, we can observe that the nanogap width has little variation from the side to the middle in this array although the etched parts under the nanogap have an evident difference between the side and middle of this nanogap array. To explain this phenomenon, the displacement distribution in a nanogap array after the stress was released was simulated by FEM, as shown in Fig. 2d, suggesting that the nanobridges in an array coupled with each other; this led to an almost uniform width in an array. Fig. 2e indicates a better agreement between the simulated (black rectangle) and experimental (empty circle) results for gap width in the array shown in Fig. 2c. Although the gap width in the sides is only approximately 6% larger than that at the center, the nanogaps in an array still show significant uniformity.

The dependencies of the SiN$_x$ nanogap on the length and width of the nanobridge are summarized in Fig. 2f. We can see that the nanogap increases with the increasing bridge length at a fixed bridge width, but an inverse trend is seen in which the nanogap decreases with the increasing bridge width at a fixed bridge length. As the bridge length varies, the sample with a 20 nm wide bridge changes more than the other samples; this indicates that a narrower bridge width is more critical to nanogap formation when the bridge length varies. Therefore, this cracking-induced nanogap depends on the variation in the shape of the nanobridges controlled by not only their length, but also width; this is very different from that reported in a previous study.[40] In this study, we proposed that the shape of the nanobridge depended on its length (X) and width (Y) defined in Fig. 2a, determining the width of the SiN$_x$ nanogap (W). When the Si substrate below the nanobridge is etched along both vertical and lateral directions, the concentration and release of stress lead to the formation of a nanogap, and its width (W) can be expressed as: $W = \sigma \cdot S(X,Y) \cdot (1-\upsilon)/E$. In this equation, σ, E, and υ are the stress, Young's Modulus, and Poisson's ratio of the SiN$_x$ film, respectively, and $S(X, Y)$ is a shape function that is related to the length (X) and width (Y) of the nanobridge and determines the size of the
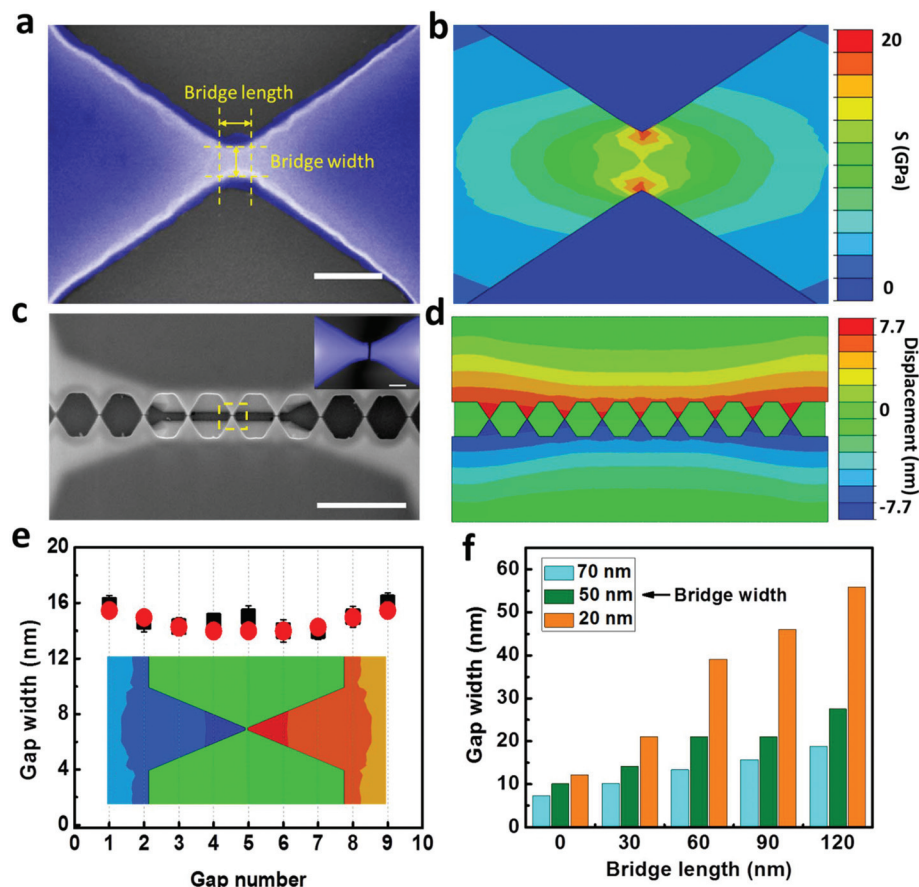
Fig. 2 (a) An SEM image of a single SiN$_x$ nanobridge before the TMAH etching process, in which the shape of the nanobridge is determined by its width and length defined by the dashed line. Scale bar 100 nm. (b) Maximum principal stress distribution of this single nanobridge. (c) An SEM image of a typical suspended SiN$_x$ nanogap array with 9 nanogaps after the etching process, in which the stress has been released. The inset shows an enlarged single nanogap in the middle of this array, as marked by a dashed line. Scale bar 2 μm and 100 nm. (d) The simulated displacement distribution in this nanogap array corresponding to (c). (e) A comparison of the results obtained from the simulated (black rectangle) and experimental (empty circle) width of each gap in this array. The inset shows a magnified view of the single SiN$_x$ gap selected from (d). (f) Nanogap width (W) as a function of the width (X) and length (Y) of the nanobridge.

etched area below the nanobridge. Practically, with the increasing bridge length (X) and decreasing bridge width (Y), more Si below the nanobridge can be etched away, $S(X, Y)$ tends to be larger, and consequently, the gap width (W) enlarges. Thus, the gap width can be well defined by $S(X, Y)$, controlling the etched amount of Si below the nanobridge; moreover, this explains the variation mechanism of the nanogap with the length and width of the nanobridge, as shown in Fig. 2d.

Metallization is a key step to functionalize SiN$_x$ nanogaps and form metal nanogaps. Herein, a high-quality smooth Ag film with a roughness of 2.3 nm (RMS) is coated on the SiN$_x$ nanogap arrays for metallization. The Ag deposition can narrow the SiN$_x$ nanogap to sub-10 nm by partly filling it with a Ag film; this finally forms the desired Ag/SiN$_x$ nanogap. Fig. 3a shows the comparison of the width of the SiNx nanogap in a single array with 9 gaps before and after Ag deposition, and this array is chosen freely from the large-area nanogap arrays shown in Fig. 1c and d. We can see that 9 SiN$_x$ nanogaps with the same width of ~30 nm in one array (blue column) can be shrunk to a sub-10 nm gap (red column) by depositing a ~25 nm thick Ag layer; this reflects the uniformity and reliability of this metallization process. Moreover, SiN$_x$ gaps, with different widths in the range of 20–50 nm, can be tuned to form sub-10 nm metallic nanogaps by adjusting the thickness of the Ag coating between 20 and 60 nm, as shown in Fig. 3b; this indicates a linear dependence of the metal gap width on the SiN$_x$ gap at different Ag thicknesses. Fig. 3c exhibits the morphologies of three typical sub-10 nm Ag/SiN$_x$ nanogaps, *i.e.* 7.8 nm, 8.5 nm, and 9.6 nm, selected from Fig. 3b. We can see that the SiN$_x$ gaps of various sizes can be shrunk down to sub-10 nm by controlling Ag deposition; this implies the stability and controllability of this metallization process. Based on Fig. 1–3, we confirmed the feasibility of stress-cracking and metallization, together controlling the 3D suspended nanogaps; this further demonstrated a reproducible, scalable, and large-scale fabrication of 3D metal nanogap arrays with the width of the gaps controllable from sub-10 nm to tens of nanometers, providing a reliable, customized way to
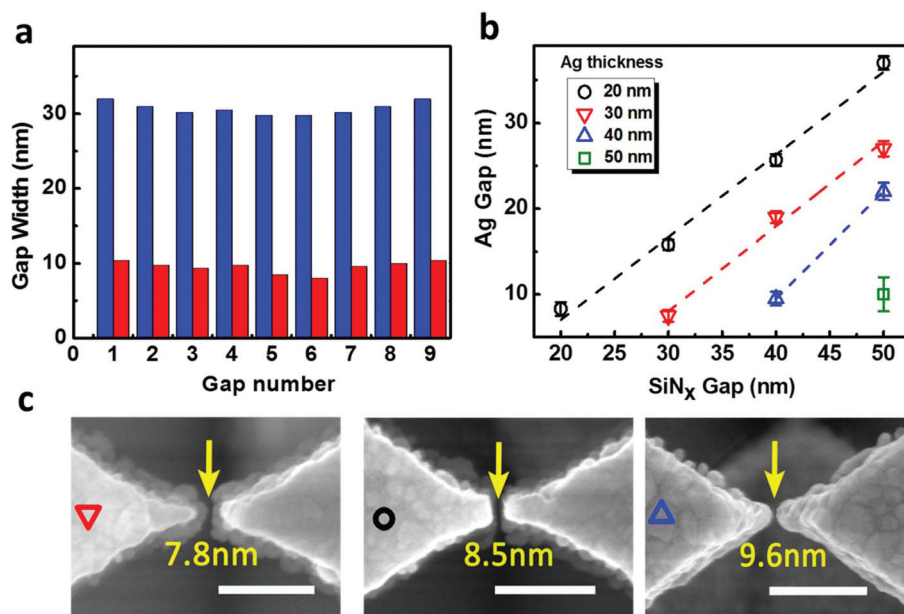
Fig. 3 (a) Statistical results of a typical SiN$_x$ nanogap array before and after Ag layer deposition; one SiN$_x$ nanogap array has 9 gaps in number and about 30 nm width, and a sub-10 nm Ag nanogap (red column) can be fabricated by depositing a 25 nm Ag layer on a SiN$_x$ nanogap (blue column). (b) Dependence of the Ag nanogap width on the width of the SiN$_x$ nanogap and the thickness of the Ag layer. (c) SEM images of sub-10 nm Ag gaps obtained on SiN$_x$ nanogaps with the widths of 20 nm, 30 nm, and 40 nm by correspondingly depositing the Ag film of 20 nm, 30 nm, and 45 nm, respectively. Scale bar: 100 nm.

mass-produce plasmonic nanogap arrays. Hence, the method as a whole is rather conducive to gap-based electronic device applications.

Suspended plasmonic nanogap array as an ultrasensitive SERS substrate

The plasmonic nanogap array structure is a perfect candidate for highly sensitive SERS detection due to strong electromagnetic field enhancement induced by the nanogap. Herein, an as-fabricated sample array of suspended 3D Ag/SiN$_x$ nanogaps of ~8 nm width is employed as an SERS probe, and Rhodamine 6G (R6G) is used as a Raman probe. Each nanogap in a single array can be used as a Raman measurement point for SERS detection with ~2 μm size in area. To obtain the sensitivity of these suspended plasmonic nanogaps as an SERS probe, the Raman spectra of R6G molecules with concentrations ranging from 10^{-8} M to 10^{-16} M on the suspended nanogaps were successively obtained, as shown in Fig. 4a. Note that the signal of R6G is still detectable at an extremely low concentration of 10^{-16} M from most nanogaps; this directly demonstrates the remarkable ability of the sub-10 nm suspended nanogaps for ultra-sensitive molecular detection. Fig. 4b shows the dependence of the intensities of two typical R6G characteristic peaks at 613 cm^{-1} and 1366 cm^{-1} on the concentration, revealing a linear dependence of intensity on concentration. To further examine the sensitivity of 3D nanogaps, the SERS spectra of R6G at 10^{-16} M on the same nanogap array were obtained after immersing for 3 h, 6 h, 9 h, and 12 h. In Fig. 4c, we can see that the intensity

of the typical R6G characteristic peaks increases gradually as the immersion time increases from 3 hours to 12 hours, and the peaks at 613 cm^{-1}, 775 cm^{-1}, and 1366 cm^{-1} become distinguishable after 6 hours and strong after 12 hours; this suggests that the number of absorbed molecules increases with time. Corresponding to Fig. 4c, the near-linear dependence of the peak intensities at 613 cm^{-1} and 1366 cm^{-1} on the immersion time is a further evidence that the nanogap array-covered surface has an ultra-sensitive capability to detect molecules, as shown in Fig. 4d. Then, the uniformity of the SERS spectra is tested by obtaining the Raman spectra for R6G in a 10^{-16} M solution from five nanogaps on a single random nanogap array, as shown in Fig. 4e, in which most typical R6G characteristic peaks can still be clearly distinguished, sufficiently demonstrating the homogeneity of the extreme detection ability of suspended nanogaps. To examine the spatial distribution of the localized field enhancement and the homogeneity of the SERS response, Raman mapping was performed on a nanogap array prepared in the R6G solution at 10^{-8} M. The Raman mapping image was obtained using the sum of peak intensities at 613 cm^{-1}, 775 cm^{-1}, and 1366 cm^{-1}. As can be seen in Fig. 4f, the mapping image is a clear profile of the nanogap array, which overlays well with the optical image. Notably, the highest SERS intensity has been found at the nanogap; this implies that the hot spots locate only in the nanogap zone. The mapping results certainly demonstrate that the strong electric field enhancement is localized entirely in the gap zone and show the controllability and repeatability of the fabrication process. In addition, we can see
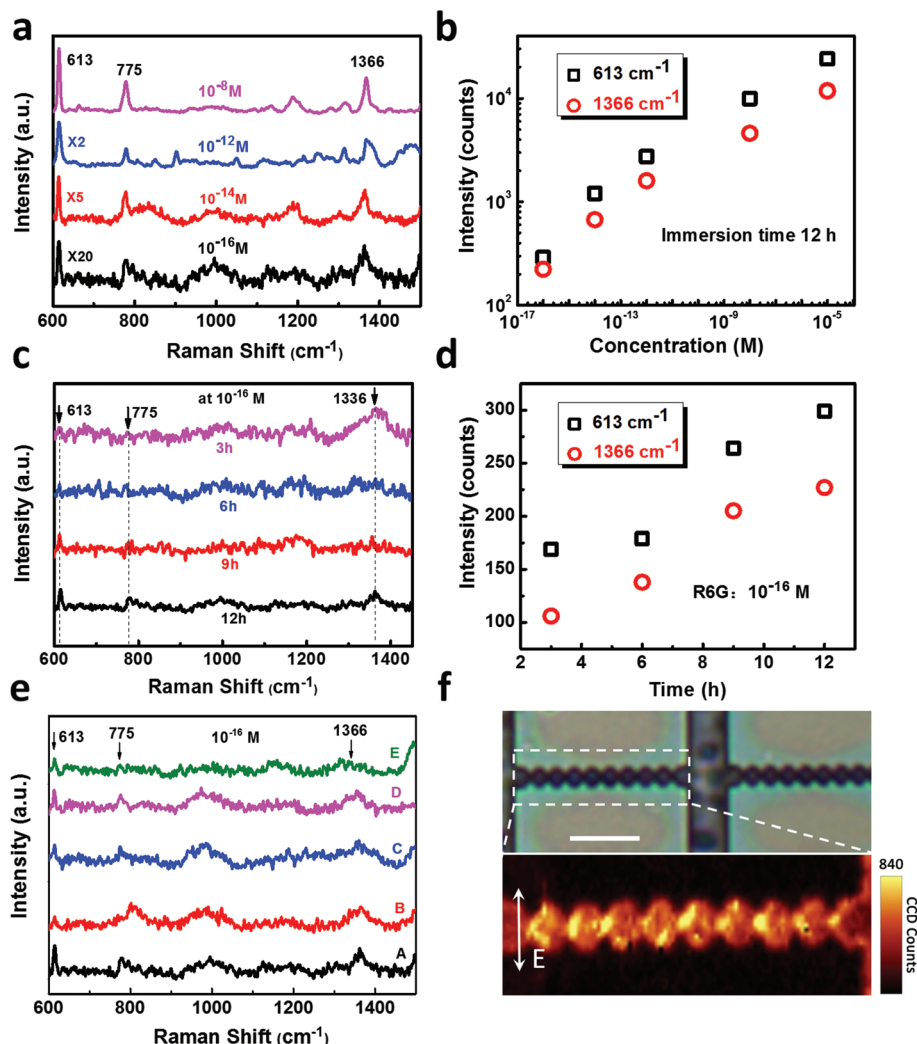
Fig. 4 (a) SERS spectra of R6G with different concentrations ranging from 10^{-8} M to 10^{-16} M, all from one single nanogap under the same immersion time. To make this graph visually clear, the spectra of 10^{-14} M and 10^{-16} M are multiplied by 5 and 20, respectively. (b) The intensity of the Raman feature peak of R6G at 613 cm^{-1} and 1366 cm^{-1} as a function of molecular concentration from 10^{-8} to 10^{-16} M (in log scale), corresponding to (a). (c) SERS spectra of the same gap with 10^{-16} M R6G were obtained after immersion for 3 h, 6 h, 9 h, and 12 h. (d) The changes in intensity of the Raman feature peaks of R6G at 613 cm^{-1} and 1366 cm^{-1} with immersion time corresponding to (c). (e) The SERS spectra obtained from five sub-10 nm nanogaps in a single random array prepared with an R6G solution of 10^{-16} M, showing good uniformity. (f) Raman optical image (top) of typical nanogap arrays and the corresponding Raman mapping image (bottom) of a nanogap array created using the sum of peak intensities at 613 cm^{-1}, 775 cm^{-1}, and 1366 cm^{-1}, with an R6G solution of 10^{-8} M. Scale bar: 2 μm.

that the areas aside the suspended nanogap structure exhibit strong SERS intensity, which can be attributed to the rough surface caused by the etching process as a result of the metallization process.

Herein, the SERS enhancement factor (EF) can be estimated by the conventional formula EF = $(I_{SERS}/N_{SERS})/(I_{Bulk}/N_{Bulk})$, where I_{SERS} and N_{SERS} are the SERS signal intensity and number of molecules absorbed on the surface of the sample exposed by the laser, respectively, and I_{Bulk} and N_{Bulk} are the Raman signal intensity and number of molecules of R6G powder exposed by the laser, respectively. The generally accepted notion is that when a sample is immersed in a 10^{-4} M R6G solution for 3 hours, a monolayer of R6G absorbs on

the sample surface.[41,42] Then, N_{SERS} can be calculated by $N_{SERS} = S/S_{R6G}$; S and S_{R6G} are the area of the sample exposed by the laser and the occupied area of a R6G molecule, respectively. Moreover, $N_{bulk} = M/m = (S_{spot} \cdot L \cdot \rho \cdot N_A)/m_{mol}$, where M and m are the mass of excited R6G powder and the molecular mass of R6G, respectively. L is the depth of laser penetration in R6G, ρ is the density of R6G, and S_{spot} is an area of laser spot with a 1 μm radius, N_A is the Avogadro's number, and m_{mol} is the molar mass of R6G. The calculated results indicate that the SERS EF of R6G in the suspended 8 nm Ag/SiN$_x$ nanogap structure can be estimated to be ~10^8, higher than the SERS EF reported using other nanofabrication processes. This high SERS EF value for a 3D nanogap is the reason that we have

obtained an extremely high sensitivity of 10^{-16} M in SERS detection while holding promise for SERS detection even at a single-molecule level.[43]

Field enhancement mechanism

For the as-fabricated 3D plasmonic nanogap, a sub-10 nm gap is a very important feature that can produce a very strong field enhancement effect that contributes mainly to ultrasensitive detection. Moreover, a large ratio of gap-height to gap-width (more than 30) is another outstanding feature, which forms a deep nanocavity below the Ag-nanogap to confine photons and further increase the field enhancement in the gap zone. Thus, this deep plasmonic nanogap will have an advantage in local field enhancement over a shallow nanogap. Fig. 5 shows the FDTD simulation results of the electromagnetic field distribution of a sub-10 nm suspended 3D Ag/SiN$_x$ gap, clarifying

the mechanism of field enhancement and the concentrated effect on the light in a deep nanocavity below the nanogap. As shown in Fig. 5a, the 8 nm metallic nanogap formed by coating a 25 nm Ag layer over a SiN$_x$ nanogap with a depth of 220 nm was chosen as a basic model structure. Fig. 5b illustrates the field distribution on a suspended Ag/SiN$_x$ nanogap above a V-shaped cavity, and herein, we can see clearly that the maximum value of the enhanced field is localized entirely between two Ag tips. Fig. 5c and d shows the X–Z and X–Y enlarged views, respectively, of the electric field amplitude distribution in a single Ag-nanogap, in which the strongest field enhancement clearly appears in the top of the Ag nanogap and in the center between Ag tips, greatly contributing to ultrasensitive SERS detection. Moreover, the Ag nanoparticles around the nanogap have contribution to the SERS effect. The depth of the SiN$_x$ gap, with a high aspect ratio forming a verti-
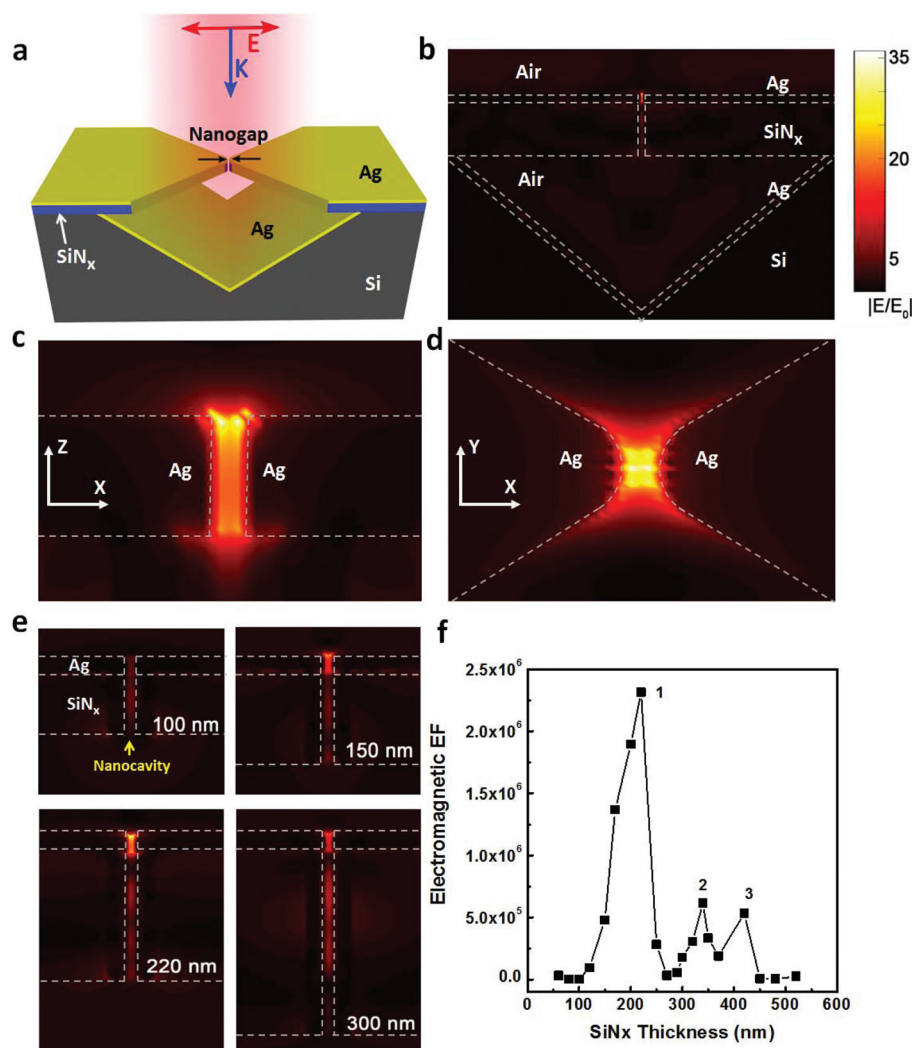
Fig. 5 (a) Schematic of the structure of the 3D suspended Ag/SiN$_x$ nanogap. (b) Cross-sectional view of the calculated electric field distribution in a suspended Ag/SiN$_x$ nanogap. (c) and (d) magnified X–Z and X–Y views of the electric field distribution in the Ag nanogap, respectively. (e) Electric field distribution profiles of the suspended Ag/SiN$_x$ nanogap with 100 nm, 150 nm, 220 nm, and 300 nm thick SiN$_x$ layer, respectively. (f) Dependence of the field enhancement factor (EF) of the Ag nanogap on SiN$_x$ layers of different thicknesses, indicating the Fabry–Perot resonance occurring in this nanocavity structure.

cal nanocavity, must be another key factor influencing the field enhancement of the suspended Ag nanogap. It has been demonstrated that the nanocavity structure helps magnify the electric field coupling in the nanogap[23,44] by squeezing the phonon into a small volume. Thus, this nanocavity enhances the plasmon coupling in the gap zone, leading to a higher SERS intensity in the nanogap.

In this study, the depth of a nanocavity is determined by the thickness of the SiN_x layer. Fig. 5e presents the FDTD simulation results of field distribution at different thicknesses from 100 nm to 300 nm of the SiN_x layer, one-to-one corresponding to the depth of the SiN_x gap; thus, we can clearly distinguish the effect of the SiN_x gap depth on the field enhancement of the Ag nanogap by brightness differences of the spots dispersed in the nanocavity. By examining the field distribution along the Ag/SiN_x gap, we can see that a gap depth of 220 nm shows the strongest field intensity, focused mainly around the upper end of the gap. Moreover, the field intensity distribution along the gap varies somewhat in brightness with change in the gap depth. Overall, this trench is covered with Ag and forms a gap line *via* two slanted side walls, which can generate a strong local electric field and couple with LSPR from the nanogap of the top Ag. Further, we infer that this nanocavity can be considered as a nano-waveguide structure composed of the upper Ag nanogap and the lower SiN_x deep nanogap. When an incident light beam enters this nano-waveguide structure through the metal nanogap, the light produces a series of reflectance and interference effects, causing the Fabry–Perot resonance. In this kind of resonance, the field intensity distribution differs according to the gap depth at the nanocavity, which agrees well with the simulated field intensity distribution shown in Fig. 5e.

To further verify the existence of the Fabry–Perot resonance in this nanocavity, the simulated electromagnetic enhancement factor (EF) of the Ag nanogap is plotted for different SiN_x gap depths in Fig. 5f. The curve in Fig. 5f shows a clear fluctuation, and the highest EF of 2.3×10^6 appears at a gap depth of 220 nm and then decreases with the decreasing gap depth. Interestingly, two other peak values of EF can be observed at the gap depths of 340 nm and 420 nm, showing a quasi-periodic change feature. The variation of EF with gap depth, given in Fig. 5f, sufficiently complies with the characteristics of Fabry–Perot resonance to prove that this resonance occurs in this nanogap structure. For the Fabry–Perot resonance, if the depth of the nanocavity and the wavelength of the light are well matched, the EF value reaches a maximum due to a resonance dominated by constructive interference; otherwise, the EF value tends toward a minimum when the resonance is dominated by destructive interference.[24,33,45] Therefore, for these 3D suspended Ag/SiN_x nanogaps considered as plasmonic nanocavities with a high aspect ratio, an appropriate gap depth (220 nm) is highly conducive to greatly enhanced local field intensity in the nanocavity and especially in the Ag nanogap due to the Fabry–Perot resonance occurring in the nanocavity, which contributes greatly to ultrasensitive SERS detec-

tion in this study. Notably, the abovementioned simulated electromagnetic EF is smaller than the previous calculated SERS EF; this can be attributed to the fact that the electromagnetic EF simulation cannot reflect two contributions from both chemical enhancement and the rough surface of the Ag film to enhance the SERS signal as compared to the case of SERS EF.

Conclusions

In this study, we present a feasible approach to fabricate sub-10 nm suspended plasmonic metallic nanogaps with extreme geometries by combining stress-induced cracking with metallization. The fabrication method has good controllability for the location, number, and size of nanogap formation in a large area and can produce large numbers of nanogap array devices on a surface with good uniformity. This 3D plasmonic nanogap is used as an SERS substrate, showing an extremely high sensitivity of $\sim 10^{-16}$ M to R6G molecules and a very strong SERS enhancement factor of $\sim 10^8$, demonstrating extraordinary SERS detection ability even at the single-molecule level and great potential for application in ultra-sensitive detection devices. Interestingly, based on FDTD simulation, we can find that the Fabry–Perot resonance occurs in a deep nanocavity beneath the nanogap structure that greatly enhances the local field intensity, especially in the Ag nanogap sample with the highest electromagnetic EF of 2.3×10^6, at a gap depth of 220 nm and is the main contributor to the ultrasensitive SERS detection demonstrated in this study. Moreover, this 3D metallic nanogap is a good candidate for nanoelectrodes serving as building blocks for electronic measurement devices. The nanocracking followed by metallization was proven to be a stable, repeatable, and efficient way to fabricate suspended sub-10 nm gaps over a large area and opens a route for the practical application of these arrays in molecular devices and sensing and even more promising areas.

Conflicts of interest

The authors declare no competing financial interest.

Acknowledgements

References

1 J. Semple, S. Rossbauer, C. H. Burgess, K. Zhao, L. K. Jagadamma, A. Amassian, M. A. McLachlan and T. D. Anthopoulos, *Small*, 2016, **12**, 1993–2000.

2 W. Zhu, M. G. Banaee, D. Wang, Y. Chu and K. B. Crozier, *Small*, 2011, **7**, 1761–1766.

3 S. Si, W. Liang, Y. Sun, J. Huang, W. Ma, Z. Liang, Q. Bao and L. Jiang, *Adv. Funct. Mater.*, 2016, **26**, 8137–8145.

4 M. Parzefall, P. Bharadwaj, A. Jain, T. Taniguchi, K. Watanabe and L. Novotny, *Nat. Nanotechnol.*, 2015, **10**, 1058–1063.

5 H. Song, M. A. Reed and T. Lee, *Adv. Mater.*, 2011, **23**, 1583–1608.

6 J. O. Lee, Y. H. Song, M. W. Kim, M. H. Kang, J. S. Oh, H. H. Yang and J. B. Yoon, *Nat. Nanotechnol.*, 2013, **8**, 36–40.

7 Q. Zhao, W. Wang, J. Shao, X. Li, H. Tian, L. Liu, X. Mei, Y. Ding and B. Lu, *Adv. Mater.*, 2016, **28**, 6337–6344.

8 W. Cai, J. S. White and M. L. Brongersma, *Nano Lett.*, 2009, **9**, 4403.

9 T. Yelin, R. Korytar, N. Sukenik, R. Vardimon, B. Kumar, C. Nuckolls, F. Evers and O. Tal, *Nat. Mater.*, 2016, **15**, 444–449.

10 M. Di Ventra and M. Taniguchi, *Nat. Nanotechnol.*, 2016, **11**, 117–126.

11 B. Jang, K. Y. Lee, J.-S. Noh and W. Lee, *Sens. Actuators, B*, 2014, **193**, 530–535.

12 L. V. Brown, X. Yang, K. Zhao, B. Y. Zheng, P. Nordlander and N. J. Halas, *Nano Lett.*, 2015, **15**, 1272–1280.

13 D. Kang, P. V. Pikhitsa, Y. W. Choi, C. Lee, S. S. Shin, L. Piao, B. Park, K. Y. Suh, T. I. Kim and M. Choi, *Nature*, 2014, **516**, 222–226.

14 Z. Hu, Z. Liu, L. Li, B. Quan, Y. Li, J. Li and C. Gu, *Small*, 2014, **10**, 3933–3942.

15 J. Leem, M. C. Wang, P. Kang and S. Nam, *Nano Lett.*, 2015, **15**, 7684–7690.

16 A. Toma, S. Tuccio, M. Prato, F. De Donato, A. Perucchi, P. Di Pietro, S. Marras, C. Liberale, R. Proietti Zaccaria, F. De Angelis, L. Manna, S. Lupi, E. Di Fabrizio and L. Razzari, *Nano Lett.*, 2015, **15**, 386–391.

17 C. Zhu, G. Meng, P. Zheng, Q. Huang, Z. Li, X. Hu, X. Wang, Z. Huang, F. Li and N. Wu, *Adv. Mater.*, 2016, **28**, 4871–4876.

18 J. Zhang, M. Irannejad and B. Cui, *Plasmonics*, 2014, **10**, 831–837.

19 N. A. Hatab, C. H. Hsueh, A. L. Gaddis, S. T. Retterer, J. H. Li, G. Eres, Z. Zhang and B. Gu, *Nano Lett.*, 2010, **10**, 4952–4955.

20 D. Natelson, Y. Li and J. B. Herzog, *Phys. Chem. Chem. Phys.*, 2013, **15**, 5262–5275.

21 X. Liu, D. Wu, Q. Chang, J. Zhou, Y. Zhang and Z. Wang, *Nanoscale*, 2017, **9**, 15390–15396.

22 Z. Xie, S. Feng, P. Wang, L. Zhang, X. Ren, L. Cui, T. Zhai, J. Chen, Y. Wang and X. Wang, *Adv. Opt. Mater.*, 2015, **3**, 1232–1239.

23 M. K. Kim, H. Sim, S. J. Yoon, S. H. Gong, C. W. Ahn, Y. H. Cho and Y. H. Lee, *Nano Lett.*, 2015, **15**, 4102–4107.

24 X. Chen, H. R. Park, M. Pelton, X. Piao, N. C. Lindquist, H. Im, Y. J. Kim, J. S. Ahn, K. J. Ahn, N. Park, D. S. Kim and S. H. Oh, *Nat. Commun.*, 2013, **4**, 2361.

25 S. Chen, S. Jin and R. Gordon, *Phys. Rev. X*, 2014, **4**, 031021.

26 N. A. Abu Hatab, J. M. Oran and M. J. Sepaniak, *ACS Nano*, 2008, **2**, 377–385.

27 W. Yue, Y. Yang, Z. Wang, L. Chen and X. Wang, *J. Phys. Chem. C*, 2013, **117**, 21908–21915.

28 A. Otto, *J. Raman Spectrosc.*, 2006, **37**, 937–947.

29 J. Chen, G. Qin, J. Wang, J. Yu, B. Shen, S. Li, Y. Ren, L. Zuo, W. Shen and B. Das, *Biosens. Bioelectron.*, 2013, **44**, 191–197.

30 H. Lee, G. H. Kim, J. H. Lee, N. H. Kim, J. M. Nam and Y. D. Suh, *Nano Lett.*, 2015, **15**, 4628–4636.

31 X. Chen, N. C. Lindquist, D. J. Klemme, P. Nagpal, D. J. Norris and S. H. Oh, *Nano Lett.*, 2016, **16**, 7849–7856.

32 Q. Xiang, X. Zhu, Y. Chen and H. Duan, *Nanotechnology*, 2016, **27**, 075201.

33 D. Yoo, N. C. Nguyen, L. Martin-Moreno, D. A. Mohr, S. Carretero-Palacios, J. Shaver, J. Peraire, T. W. Ebbesen and S. H. Oh, *Nano Lett.*, 2016, **16**, 2040–2046.

34 J. Zhao, M. Sun, Z. Liu, B. Quan, C. Gu and J. Li, *Sci. Rep.*, 2015, **5**, 16019.

35 S. Marqués-González, R. Matsushita and M. Kiguchi, *J. Opt.*, 2015, **17**, 114001.

36 H. Ni, M. Wang, T. Shen and J. Zhou, *ACS Nano*, 2015, **9**, 1913–1925.

37 L. Lesser-Rojas, P. Ebbinghaus, G. Vasan, M. L. Chu, A. Erbe and C. F. Chou, *Nano Lett.*, 2014, **14**, 2242–2250.

38 J. Tian, B. Liu, X. Li, Z. Yang, B. Ren, S. Wu, N. Tao and Z. Tian, *J. Am. Chem. Soc.*, 2006, **128**, 14748.

39 S. Pud, D. Verschueren, N. Vukovic, C. Plesa, M. P. Jonsson and C. Dekker, *Self-Aligned Plasmonic Nanopores by Optically Controlled Dielectric Breakdown*, 2015.

40 V. Dubois, F. Niklaus and G. Stemme, *Adv. Mater.*, 2016, **28**, 2178–2182.

41 J. Chen, B. Shen, G. Qin, X. Hu, L. Qian, Z. Wang, S. Li, Y. Ren and L. Zuo, *J. Phys. Chem. C*, 2012, **116**, 3320–3328.

42 W. Yue, Z. Wang, J. Whittaker, F. Lopez-royo, Y. Yang and A. V. Zayats, *J. Mater. Chem. C*, 2017, **5**, 4075–4084.

43 E. C. Le Ru and P. G. Etchegoin, *Annu. Rev. Phys. Chem.*, 2012, **63**, 65–87.

44 M. Chirumamilla, A. Toma, A. Gopalakrishnan, G. Das, R. P. Zaccaria, R. Krahne, E. Rondanina, M. Leoncini, C. Liberale, F. De Angelis and E. Di Fabrizio, *Adv. Mater.*, 2014, **26**, 2353–2358.

45 H. T. Miyazaki and Y. Kurokawa, *Phys. Rev. Lett.*, 2006, **96**, 097401.